

## Chandra’s insights into SN 2023ixf\*

POONAM CHANDRA,<sup>1</sup> ROGER A. CHEVALIER,<sup>2</sup> KEIICHI MAEDA,<sup>3</sup> ALAK K. RAY,<sup>4</sup> AND NAYANA A.J.<sup>5</sup>

<sup>1</sup>*National Radio Astronomy Observatory, 520 Edgemont Rd, Charlottesville VA 22903, USA*

<sup>2</sup>*Department of Astronomy, University of Virginia, Charlottesville VA 22904-4325, USA*

<sup>3</sup>*Department of Astronomy, Kyoto University, Kitashirakawa-Oiwake-cho, Sakyo-ku, Kyoto, 606-8502, Japan*

<sup>4</sup>*Homi Bhabha Centre for Science Education, TIFR, Mumbai 400088, India*

<sup>5</sup>*Department of Astronomy, University of California, Berkeley, CA 94720-3411*

### ABSTRACT

We report *Chandra*-ACIS observations of SN 2023ixf in M101 on day 13 and 86 since the explosion. The X-rays in both epochs are characterized by high temperature plasma from the forward shocked region as a result of circumstellar interaction. We are able to constrain the absorption column density at both *Chandra* epochs, which is much larger than that due to the Galactic and host absorption column, and we attribute it to absorption by the circumstellar matter in the immediate vicinity of SN 2023ixf. Combining our column density measurements with the published measurement on day 4, we show that the column density declines as  $t^{-2}$  between day 4 to day 13 and then evolves as  $t^{-1}$ . The unabsorbed 0.3 – 10 keV luminosity evolves as  $t^{-1}$  during the *Chandra* epochs. On day 13 *Chandra* observation we detect the Fe K- $\alpha$  fluorescent line at 6.4 keV indicating presence of cold material in the vicinity of the SN. The line is absent on day 86, consistent with the decreased column density by a factor of 7 between the two epochs. Our analysis indicates that during 10 years to 1.5 years before explosion, the progenitor was evolving with a constant mass-loss rate of  $5.6 \times 10^{-4} M_{\odot} \text{ yr}^{-1}$ .

*Keywords:* Stellar mass loss (1613) — Core-collapse supernovae (304) — Circumstellar matter (241)  
— X-ray transient sources (1852)

### 1. INTRODUCTION

Understanding and mapping the progenitors to their core-collapse supernovae (CCSNe) is one of the biggest challenges in stellar astronomy. An important component tying CCSNe to their massive progenitors is an understanding of stellar mass-loss during the final evolutionary phases, forming the circumstellar material (CSM) surrounding the star, which can dramatically alter the observable properties of a supernova (SN). One of the major developments in this field is the indication that most progenitors undergo the enhanced mass-loss just before explosions, evidence of which has been seen observationally via “flash” spectroscopy (e.g. Gal-Yam et al. 2014; Yaron et al. 2017; Kochanek 2019, etc.). While it is not entirely clear, the mass-loss could be enhanced via several mechanisms, including, but not limited to, nuclear burning instabilities (Smith & Arnett

2014) and gravity wave driven mass-loss (Quataert & Shiode 2012).

SN 2023ixf is the closest Type II SN observed in decades and, hence, provides an excellent opportunity to study its properties in detail. It was discovered on 2023 May 19.73 UT in the nearby galaxy M101 by an amateur astronomer Koichi Itagaki (Itagaki 2023) and was quickly classified as a Type II supernova (Perley et al. 2023). Later it was further classified as a Type IIL SN (Bianciardi et al. 2023). Hiramatsu et al. (2023) estimated the explosion date to be  $\text{MJD} = 60082.743 \pm 0.083$  (2023 May 18.75 UT), corresponding to 0.98 days before the discovery. We adopt this explosion date throughout the paper.

Due to the proximity, detailed observations of SN 2023ixf have been possible in several wavebands. In addition, M101 is a well observed galaxy with a rich archival pre-explosion dataset. The pre- and post-explosion dataset have provided important insights into the progenitor of SN 2023ixf. The pre-explosion images have revealed the progenitor star to be a red supergiant

\* Released on January, 25, 2024

in a dusty region (Jencson et al. 2023; Kilpatrick et al. 2023; Soraisam et al. 2023; Van Dyk et al. 2023). Several groups have constrained the mass of the progenitor, which have resulted so far in a large mass range within 8–20  $M_{\odot}$  (Pledger & Shara 2023; Kilpatrick et al. 2023; Jencson et al. 2023; Soraisam et al. 2023; Niu et al. 2023).

The optical light curve of SN 2023ixf is characterized by a sharp rise to peak in 5 days from absolute magnitude  $-M_V = 10$  mag to  $M_V = -18$  and then a plateau phase lasting for 30 days at magnitude  $-17.6$  followed by a smooth decay (Hiramatsu et al. 2023; Singh Teja et al. 2023). The data have revealed prominent flash features of hydrogen, helium, carbon, and nitrogen in the spectra up to 5 days (Yamanaka et al. 2023; Jacobson-Galan et al. 2023; Smith et al. 2023; Bostroem et al. 2023; Singh Teja et al. 2023; Hiramatsu et al. 2023). The UV data along with the flash features indicate a temperature rise which is not expected in a pure-shock cooling event, indicating a delayed shock breakout in a dense CSM (Zimmerman et al. 2023; Hiramatsu et al. 2023). Vasylyev et al. (2023) measured high polarization and rapid evolution during 2–15 days, and explained it as asymmetric ejecta coming out of dense asymmetric CSM, suggesting a highly asymmetric mass-loss process.

The early X-ray emission was reported by *NuSTAR* within 4 days (Grefenstette et al. 2023), whereas the first radio detection occurred on 2023 Jun 17, around a month after explosion (10 GHz flux density  $41 \pm 8 \mu\text{Jy}$ , Matthews et al. 2023). Berger et al. (2023) reported a non-detection in millimeter bands at 2.6–18.6 days post-explosion.

There are various mass-loss estimates in the literature. Based on flash ionization features, Jacobson-Galan et al. (2023); Zimmerman et al. (2023); Bostroem et al. (2023) have determined an enhanced mass-loss rate of  $\sim 10^{-2} M_{\odot} \text{ yr}^{-1}$  just before explosion and indicated the existence of the confined CSM at  $< 10^{15}$  cm. The light curve modeling has provided even a higher mass-loss rate (e.g., Hiramatsu et al. 2023). Based on H-alpha evolution, Zhang et al. (2023) have estimated mass-loss rate of  $6 \times 10^{-4} M_{\odot} \text{ yr}^{-1}$ , 2–3 years before explosion. Soraisam et al. (2023) found a mass-loss rate of  $(2-4) \times 10^{-4} M_{\odot} \text{ yr}^{-1}$  using 19 years of archival IR data, which was also obtained by Grefenstette et al. (2023) in their X-ray *NuSTAR* measurements. On the lower end, Jencson et al. (2023) and Niu et al. (2023) estimated it to be  $(3-30) \times 10^{-5} M_{\odot} \text{ yr}^{-1}$ , and  $10^{-5} M_{\odot} \text{ yr}^{-1}$ , respectively, in 3–20 years before explosion. The metallicity has ranged between half the solar Niu et al. (2023) to solar (Van Dyk et al. 2023; Zimmerman et al. 2023).

We present here *Chandra* X-ray observations of SN 2023ixf providing us the opportunity to constrain the evolution of the progenitor. We adopt a distance of 6.85 Mpc (Riess et al. 2022), a Milky Way extinction of  $E(B - V)_{\text{MW}} = 0.0077$  mag (Schlafly & Finkbeiner 2011), and a host galaxy extinction of  $E(B - V)_{\text{host}} = 0.033$  (Lundquist et al. 2023; Smith et al. 2023; Jacobson-Galan et al. 2023; Hiramatsu et al. 2023). We also adopt a standard extinction law with  $R_V = 3.1$  (Cardelli et al. 1989).

## 2. OBSERVATIONS

SN 2023ixf was observed with the *Chandra* under the approved DDT program 24508911 (PI: Chandra). The first observations took place on 2023 May 31 15:34:04 UT for 20.3 ks. The second set of observations was conducted on 2023 Aug 11 18:17:07 and 2023 Aug 12 12:07:33 UT with 11.18 and 10.02 ks, respectively. The observations were taken with ACIS-S without grating in a VFaint mode. We extracted the spectra using CIAO software<sup>1</sup> version 4.15 and used *xspec* under HEASOFT<sup>2</sup> version 6.31 to carry out the spectral analysis. For the second epoch, the individually processed spectra on Aug 11 and 12 were combined using *combine\_spectra*. A total of 720 counts were obtained in May 2023 spectrum and 233 counts in Aug 2023 in about 20 ks of exposure at each epoch.

For the May 2023 spectral fits, initially we fit the optically thin ionized plasma model absorbed with a column density. We fit the data assuming solar metallicity. While the column density is well constrained, the best fit temperature ( $\sim 60$  keV) is not constrained towards the upper end (Fig. 1). That is most likely the case when the plasma temperature is high as the *Chandra* energy range is not sensitive to such high plasma temperature. We note that Grefenstette et al. (2023) constrained the plasma temperature to 34 keV at around 29th May based on *NuSTAR* data (day 11), which is within 2 days of our first epoch. Thus we fix the plasma temperature to 34 keV in our fits. We also see an excess of flux around 6–7 keV, though not captured in the plasma model. We add a Gaussian to fit the excess flux. While the line width is not constrained due to poor energy resolution of *Chandra* the best fit line energy is  $\sim 6.4$  keV, which matches with the Iron  $K\alpha$  line energy, and is also seen in the *NuSTAR* data. We freeze the line width to 0.2 keV (see §3 for the details). The line energy is  $6.43^{+0.19}_{-0.20}$  keV (Fig. 1). Our best fit column density is  $2.50^{+0.40}_{-0.34} \times 10^{22} \text{ cm}^{-2}$ . Our value is

<sup>1</sup> <http://asc.harvard.edu/ciao/>

<sup>2</sup> <http://heasarc.gsfc.nasa.gov/docs/software/lheasoft/>

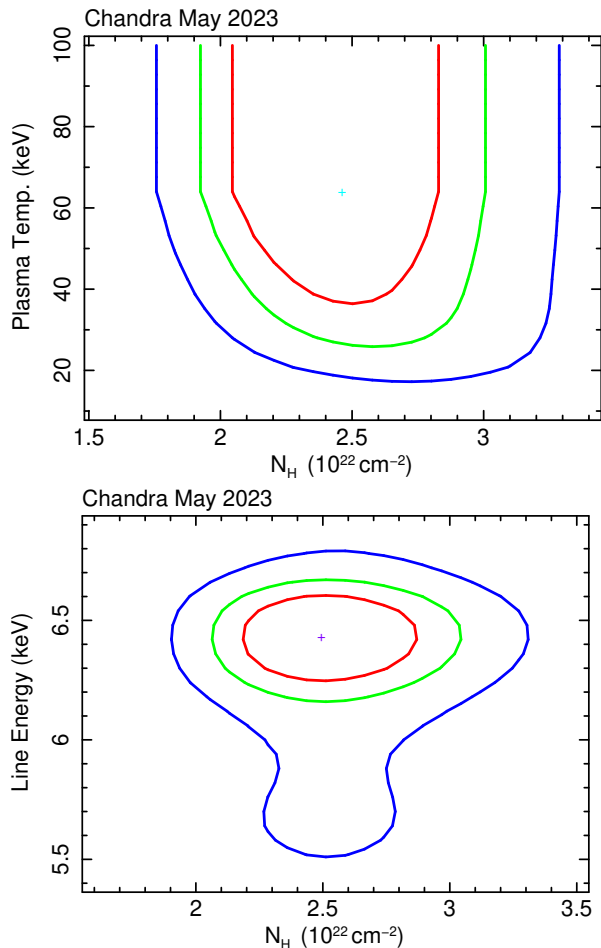


**Figure 1.** *Left:* Contour plot of the best fit parameter values of the column density and the plasma temperature for the May 2023 *Chandra* spectrum. The column density is well constrained while the temperature is not. *Right:* Contour plot of the best fit values of the Gaussian line energy and the column density. Both parameters are well constrained.

slightly smaller than that in the *NuSTAR* data on day 11 ( $5.6 \pm 2.7$ )  $\times 10^{22}$   $\text{cm}^{-2}$ ), though consistent within error bars.

In the second spectrum, we again start with fitting the absorbed plasma model and allow both the temperature and column density to vary. There may be a hint of temperature becoming lower than the first epoch (best fit temperature  $\sim 10$  keV); however, due to limited energy range of *Chandra*, it is not possible to constrain the upper bound of the temperature (Fig. 2). As discussed in §3, we freeze the temperature to 21 keV. The column density is well constrained at this epoch and has substantially decreased to  $0.36^{+0.22}_{-0.17} \times 10^{22}$   $\text{cm}^{-2}$  (Fig. 3). We do not see evidence of the 6.4 keV line at this epoch. We discuss this further in §3. In Fig. 3, we plot the best fit spectra at both epochs.

### 3. RESULTS AND DISCUSSION

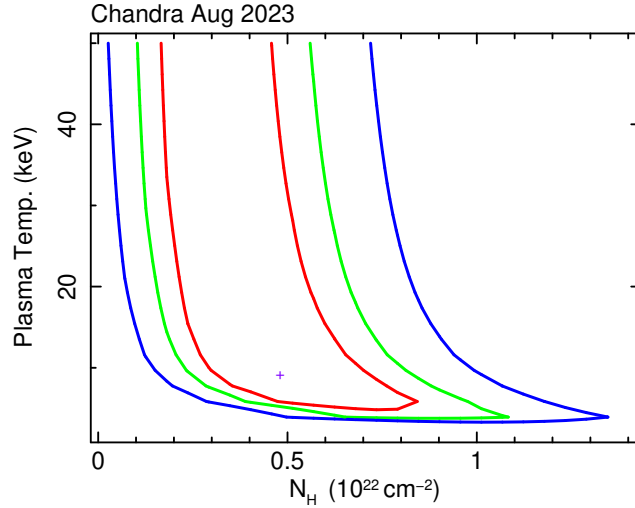
#### 3.1. *SN 2023ixf* X-ray characteristics

Table 1 lists the best fit model parameters and the derived flux values. Due to the limited energy range, the *Chandra* observations could not constrain the plasma temperature. We use the temperature of 34 keV in the first spectrum, as obtained in the nearly coincident *NuSTAR* data (Grefenstette et al. 2023). As discussed below, we find that during the *Chandra* observation epochs, the column density and the luminosity evolution follow the standard wind scenario under constant mass-loss rate  $\rho \propto r^{-2}$  (Chevalier & Fransson 2017). Based on this we scale temperature to  $t^{-2/(n-2)}$  (where  $n$  is the power-law index of the ejecta density profile Chevalier & Fransson 2017).

If we assume  $n \sim 10$ , the temperature should evolve as 34 keV  $(t/13 \text{ day})^{-0.25}$ . Thus at the second epoch the temperature should be 21 keV. While the temperature may only be approximate, this does not introduce significant errors in our modeling. We find that for a 20% change in the plasma temperature, the column density changes by only 5% and the flux normalization changes by 1.5%

The high plasma temperature likely means that the X-ray emission is arising from the forward shock. We do not see a low energy plasma. It is possible if the CSM density is high enough that a cool dense shell forms between the forward and reverse shocks and most of the lower temperature emission from the reverse shock is absorbed. In the forward shock interpretation, the shock velocity can be deduced as  $v_{\text{sh}} = (16kT/(3\mu))^{1/2} = 5000(kT/34 \text{ keV})^{1/2} \text{ km s}^{-1}$ , where  $k$  is Boltzmann’s constant and  $\mu$  is the mean particle weight which is taken to be 0.61 here. Our velocity estimate is slightly smaller than the value of 8500  $\text{km s}^{-1}$  derived by Jacobson-Galan et al. (2023), based on H $\alpha$  and H $\beta$  line profiles. This suggests that either the H $\alpha$  and H $\beta$  profiles are arising from physically distinct regions than the X-ray emission or the shock velocity is evolving to a lower value, since Jacobson-Galan et al. (2023) derived the above ejecta velocity at earlier epochs.

The extinction due to the Milky Way and the host is  $E(B - V)_{\text{MW}} = 0.0077$  and  $E(B - V)_{\text{host}} = 0.033$ , respectively. We adopt the method listed in Schlegel et al. (1998), recalibrated by Schlafly & Finkbeiner (2011), and derive  $N_{\text{MW}} = 0.45 \times 10^{20}$   $\text{cm}^{-2}$  and  $N_{\text{host}} = 1.91 \times 10^{20}$   $\text{cm}^{-2}$ . Thus the total column density due to Milky Way and M101 is  $2.36 \times 10^{20}$   $\text{cm}^{-2}$ . The column densities derived at the two *Chandra* epochs are  $2.50 \times 10^{22}$   $\text{cm}^{-2}$  and  $0.36 \times 10^{22}$   $\text{cm}^{-2}$ , respectively,



**Figure 2.** Contour plot of the best fit parameter values for the column density and the plasma temperature for the Aug 2023 *Chandra* spectrum. The column density is well constrained while the temperature is not.

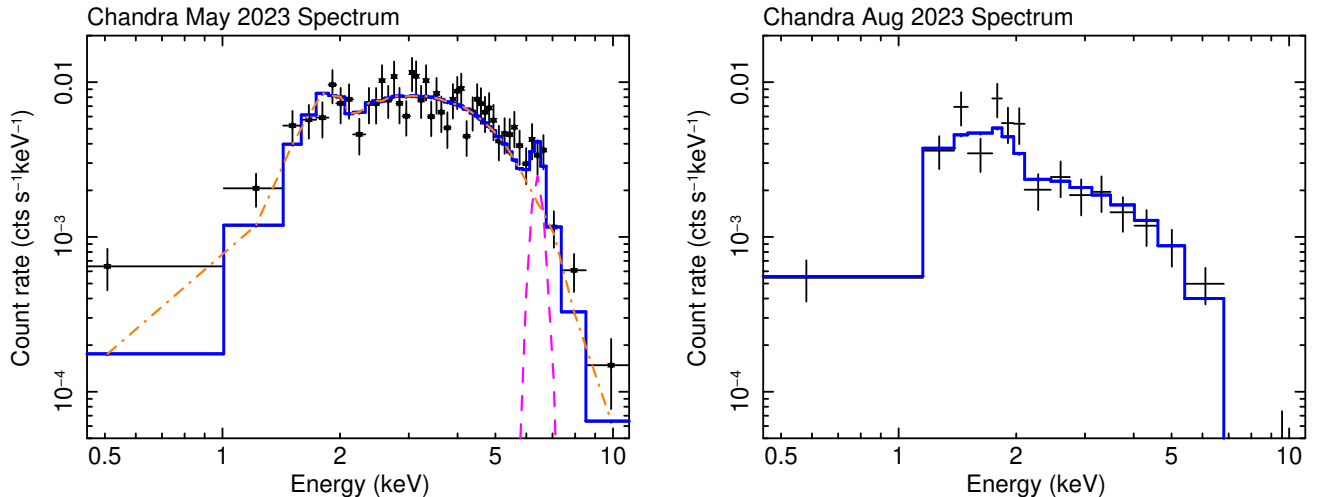


**Figure 3.** Left: May 2023 best fit spectrum of SN 2023ixf. The model is fit with an absorbed plasma with a Gaussian profile. Right: Aug 2023 best fit spectrum of SN 2023ixf. The 6.4 Fe K $\alpha$  line is no longer detected.

which are around 130 and 20 times larger than that in the direction of M101. Thus most of the column density is due to the presence of not-completely-ionized material in the vicinity of the CSM. The column density evolves as  $t^{-1.03 \pm 0.29}$  between days 13 and 86, suggesting that the wind corresponding to the CSM seen between these epochs evolved with the standard  $r^{-2}$  dependence, where  $r$  is the CSM distance from the SN explosion center. However, if one combines this along with the column density obtained in the *NuSTAR* early data on day 4, it appears that the column density decreased faster between day 4 and 13 with  $t^{-2}$  before starting to follow  $t^{-1}$  evolution (Fig. 4). This is consistent with the confined dense CSM seen via the flash ionization spectroscopy (Jacobson-Galan et al. 2023; Bostroem et al. 2023; Singh Teja et al. 2023; Smith et al. 2023; Hira-

matsu et al. 2023), and is indicative of a scenario in which the supernova underwent a very high mass-loss rate just before the explosion which resulted in a high column density on day 4, before transitioning into a low density region of a nearly constant mass-loss rate revealed around day 13 onwards (see below). The column density on day 4 from the *NuSTAR* data corresponds to an electron scattering column depth of  $\sim 0.2$ . Thus electron scattering may have been important before day 4, but not after day 4.

The flux between the two *Chandra* epochs changes by a factor of  $\sim 6$ . The unabsorbed 0.3–10.0 keV luminosity evolves at  $t^{-0.95 \pm 0.07}$  which is also consistent with the standard evolution (Chevalier & Fransson 2017). The luminosity on day 13 is  $8.53 \times 10^{39}$  erg sec $^{-1}$  which is slightly lower than the extrapolated value in the *Chan-*

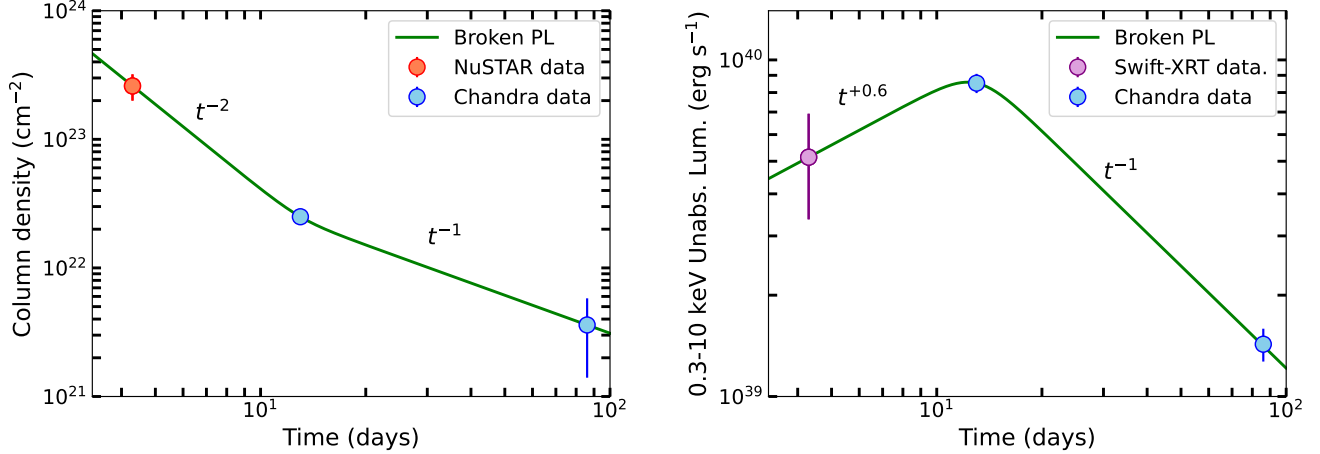


**Figure 4.** Evolution of column density (left) and 0.3–10 keV unabsorbed luminosity (right). The first red data point on day 4 in the column density plot is the *NuSTAR* data point (Grefenstette et al. 2023). The purple data point on the luminosity evolution plot is the *Swift-XRT* data point. While the column density evolves faster between day 4 and 13 before starting to follow the standard  $t^{-1}$  evolution, the 0.3–10 keV luminosity initially rises and then follows  $t^{-1}$  evolution.

**Table 1.** Spectral model fits to the SN 2023ixf spectra

	Spectrum 1	Spectrum 2
Date	2023 May 31	2023 Aug 11–12
Epoch	day $\sim$ 13	day $\sim$ 86
Exposure (ks)	20.3	21.2
Model	$N_{\text{H,tot}} \times (\text{apec} + \text{Gauss})$	$N_{\text{H,tot}} \times \text{apec}$
$N_{\text{H,tot}}$ ( $\text{cm}^{-2}$ )	$2.50^{+0.40}_{-0.34} \times 10^{22}$	$0.36^{+0.22}_{-0.17} \times 10^{22}$
apec kT (keV)	34 (fixed)	21 (fixed)
apec flux ( $\text{erg cm}^{-2} \text{s}^{-1}$ )	$1.43^{+0.09}_{-0.09} \times 10^{-12}$	$2.09^{+0.23}_{-0.23} \times 10^{-13}$
Gauss kT (keV)	$6.43^{+0.19}_{-0.20}$	...
Gauss Sigma (keV)	0.20 (fixed)	...
Gauss flux ( $\text{erg cm}^{-2} \text{s}^{-1}$ )	$1.01^{+0.45}_{-0.45} \times 10^{-13}$	...
Abs. flux ( $\text{erg cm}^{-2} \text{s}^{-1}$ )	$1.01^{+0.07}_{-0.07} \times 10^{-12}$	$2.09^{+0.23}_{-0.23} \times 10^{-13}$
Unabs. flux ( $\text{erg cm}^{-2} \text{s}^{-1}$ )	$1.53^{+0.10}_{-0.10} \times 10^{-12}$	$2.55^{+0.28}_{-0.28} \times 10^{-13}$
Unabs. $L_{0.3-10 \text{ keV}}$ ( $\text{erg sec}^{-1}$ )	$8.53^{+0.56}_{-0.56} \times 10^{39}$	$1.43^{+0.16}_{-0.16} \times 10^{39}$
$\chi^2/\nu$	1.04	0.65

*dra* energy range from the *NuSTAR* observation at day 11 ( $\sim 1.4 \times 10^{40} \text{ erg sec}^{-1}$ ), but is roughly consistent within the error bars. Panjkov et al. (2023) reported the first *Swift-XRT* detection on day 4.3 and combined the first 46 days of data to derive an unabsorbed luminosity of  $(3.0 \pm 0.7) \times 10^{39} \text{ erg sec}^{-1}$ . Since we know that parameters such as column density are evolving quickly, we do not take this approach. We combine the *Swift-XRT* measurements covering *NuSTAR* epoch 1, i.e. day 3.9–4.8 and find that there is a  $3\text{-}\sigma$  detection with 0.3–10 keV count rate of  $(1.88 \pm 0.65) \times 10^{-3} \text{ counts sec}^{-1}$ . We derive the flux using the *NuSTAR* best fit parameters on day 4, i.e.  $N_{\text{H}} = 2.6 \times 10^{23} \text{ cm}^{-2}$  and use a plasma

temperature of 34 keV (Grefenstette et al. 2023). This provides an unabsorbed (absorbed) 0.3–10 keV flux of  $(9.16 \pm 3.17) \times 10^{-13} \text{ erg cm}^{-2} \text{ s}^{-1}$  ( $(3.07 \pm 1.06) \times 10^{-13} \text{ erg cm}^{-2} \text{ s}^{-1}$ ), or an equivalent unabsorbed 0.3–10 keV luminosity of  $(5.14 \pm 1.78) \times 10^{39} \text{ erg sec}^{-1}$ . As we show in Fig. 4, the 0.3–10 keV unabsorbed luminosity initially increases between day 4 and 13 as  $t^{+0.6}$  and then evolves as  $t^{-1}$  throughout. This simply means that initially the plasma is quite hot and more emission is coming in the hard X-rays. The X-ray behaviour is qualitatively consistent with the one reported in Zimmerman et al. (2023).

Assuming that the radiation is adiabatic at *Chandra* epochs on days 13 and 86, we use equation 3.8 of Fransson et al. (1996) to calculate the mass-loss rate. We estimate the spectral luminosity at 10 keV and derive the Gaunt factor at 10 keV using Mewe et al. (1986). The mass-loss rates are  $(5.58 \pm 0.18) \times 10^{-4} M_{\odot} \text{ yr}^{-1}$  and  $(5.63 \pm 0.30) \times 10^{-4} M_{\odot} \text{ yr}^{-1}$ , on days 13 and 86, respectively. The uncertainties are only due to the flux errors. Here we assumed the forward shock velocity of  $\sim 5000 \text{ km s}^{-1}$  based on the X-ray temperature, and the wind velocity of  $115 \text{ km s}^{-1}$  based on the narrow optical line widths (Smith et al. 2023). The constant mass-loss rate between the two *Chandra* epochs is consistent with the scenario where the forward shock is moving in a wind profile of  $\rho_{\text{CSM}} \propto r^{-2}$ .

We check whether our assumption of forward shock being adiabatic is correct. In the radiative case, the luminosity of the forward shock will be  $\propto \dot{M}$ , whereas the adiabatic shock luminosity will scale as  $\propto \dot{M}^2$ . Using Chevalier & Fransson (2017), we can estimate the cooling time for the forward shock. The cooling

time scale as compared to SN age (assuming  $n = 10$  and forward shock velocity  $5000 \text{ km s}^{-1}$ ) is  $t_{\text{cool}}/t_{\text{age}} = 0.44t_{\text{age,d}}/(\dot{M}_{-4}/v_{\text{wind},2})$ . Here  $t_{\text{age,d}}$  is the SN age in days,  $\dot{M}_{-4}$  is the mass-loss rate in units of  $10^{-4} M_{\odot} \text{ yr}^{-1}$ , and  $v_{\text{wind},2}$  is the wind velocity in units  $100 \text{ km s}^{-1}$ . This means the forward shock is radiative on day 4, if the mass-loss rate is larger than  $2.2 \times 10^{-4} M_{\odot} \text{ yr}^{-1}$ . From the flash ionization spectral analysis at this epoch (e.g. [Jacobson-Galan et al. 2023](#); [Bostroem et al. 2023](#); [Hiramatsu et al. 2023](#)) and the delayed shock breakout calculation ([Zimmerman et al. 2023](#); [Hiramatsu et al. 2023](#)), the mass-loss rate is found to be of the order of  $10^{-2} M_{\odot} \text{ yr}^{-1}$ , indicating the forward shock is indeed radiative around day 4. This value for the mass-loss rate is  $\geq 10^{-3} M_{\odot} \text{ yr}^{-1}$  and  $\geq 5 \times 10^{-3} M_{\odot} \text{ yr}^{-1}$  on day 13 and 86 for the forward shock to be radiative. Our mass-loss rate estimation derived above at the *Chandra* epochs considering adiabatic expansion is self-consistent.

Assuming the column density is due to the CSM provides an independent estimate of the mass loss rate. Following [Fransson et al. \(1996\)](#), this value is  $8.7 \times 10^{-5} M_{\odot} \text{ yr}^{-1}$  at the two epochs, which is clearly smaller than the one obtained from the X-ray luminosity. The discrepancy is by a factor of 6. Even if the metallicity is half of solar metallicity, the column density will increase by only a factor of 2 and the discrepancy cannot be alleviated. This may be due to several factors like, non-spherically symmetric CSM, clumpiness, lack of electron-ion equipartition etc ([Chevalier & Fransson 2017](#)).

Based on our derived mass-loss rate and forward shock velocity, we can constrain the forward shock radius at the two *Chandra* epochs to be  $0.56 \times 10^{15} \text{ cm}$  and  $3.72 \times 10^{15} \text{ cm}$ , and the CSM density at these epochs to be  $7.84 \times 10^{-16} \text{ g cm}^{-3}$  and  $1.79 \times 10^{-17} \text{ g cm}^{-3}$ . These values are in excellent agreement with mapping of the CSM structure provided by [Zimmerman et al. \(2023\)](#).

The most likely origin of the 6.4 keV line at the first epoch, which we identified with the Fe  $K\alpha$  line, is via the fluorescent reprocessing of X-rays by the cold CSM ([Makishima 1986](#)). In this scenario the equivalent width depends upon the geometry and the iron abundance ([Matt et al. 1991](#)), and hence a good indicator of the column density. Under this scenario, a simple linear scaling between the equivalent width and column density is expected ([Torrejón et al. 2010](#)). The equivalent width in our *Chandra* measurements is 0.8 keV, which implies much larger column density than indicated by the observations. This could be due to non-spherically symmetric medium as well as the line arising from Fe of different ionization states covering wider region, par-

tially ionized plasma and farther away neutral medium ([Makishima 1986](#)).

An issue to discuss is the following: the Iron K-alpha line arises from the low ionization of Iron (i.e. Fe I to Fe XIX). For this the ionization parameter should be  $\leq 100$  ([Fabian et al. 2000](#)). Assuming the CSM is ionized by the X-rays, we can estimate the ionization parameter  $\zeta = L/nr^2$  using the X-ray luminosity and our derived mass-loss rate. The mass-loss rate derived from the X-ray luminosity corresponds to a number density of  $\sim 3.7 \times 10^8 \text{ cm}^{-3}$ . The expected ionization parameter is then around 250 at the first *Chandra* epoch. This value means that elements C, N, and O are completely ionized but heavy elements like S and Fe are not. However, at this ionization parameter, iron is likely to be ionized beyond Fe XIX as well, and will show a shift in the centroid energy, which has not been seen in our measurements. This could possibly be due to asymmetric distribution of the CSM, which has also been indicated by the spectropolarimetric data ([Vasylyev et al. 2023](#)) as well as the lack of narrow blueshifted absorption profiles in optical spectra ([Smith et al. 2023](#)).

The non-detection of Fe *Kalpha* line at the second epoch is consistent with the scenario where line originates from reprocessing of X-ray radiation via cold CSM. At the second epoch,  $N_H$  is smaller by a factor of 7, so the strength of the Fe line should be correspondingly smaller. We can make this consistency check. Under the assumption that the equivalent width of the Fe line did not change at the second epoch, the calculated line flux will be  $1.13 \times 10^{-14} \text{ erg cm}^{-2} \text{ s}^{-1}$ . At the second epoch the column density has decreased by a factor of 7. Thus a factor of 7 decrease in line strength will imply a line flux of  $1.4 \times 10^{-14} \text{ erg cm}^{-2} \text{ s}^{-1}$ , which is consistent with the calculated line flux assuming constant equivalent width.

#### 4. SUMMARY AND CONCLUSIONS

In this work we present SN 2023ixf observations with the *Chandra* ACIS-S at two epochs separated by around 2.5 months. The X-ray luminosity is arising from the adiabatic forward shock and its value ( $\sim 10^{40} \text{ erg sec}^{-1}$ ) falls somewhere in the average luminosity of core-collapse SNe ([Chandra 2018](#)). The column density and the 0.3–10 keV luminosity decline as  $t^{-1}$  during the two *Chandra* observations on day 13 and 86, indicating that the SN ejecta is expanding in the standard  $r^{-2}$  wind created by a constant mass-loss rate of  $(5.6 \pm 0.18) \times 10^{-4} M_{\odot} \text{ yr}^{-1}$  during 10–1.5 years before explosion, and is consistent with the SN 2023ixf progenitor being a massive red supergiant. The day 13 *Chandra* data also show the presence of the Fe 6.4 keV line suggesting that the CSM may not have been fully ionized

by the X-ray radiation. The line disappears on the second epoch, consistent with the decreased column density. The X-ray data indicate asymmetry in the CSM.

SN 2023ixf will be monitored for years to come and future studies will throw light on our understanding of massive stars evolving to become CCSNe at their endpoints.

## 5. ACKNOWLEDGMENTS

We thank the referee for very thoughtful comments. PC acknowledges support from NASA through Chandra award number DD3-24141X issued by the Chandra X-ray Center. RAC acknowledges support from NSF grant AST-1814910. K.M. acknowledges support from the Japan Society for the Promotion of Science (JSPS) KAKENHI grant JP18H05223, JP20H00174, and JP20H04737. The scientific results reported in this

article are based on observations made by the Chandra X-ray Observatory, data obtained from the Chandra Data Archive, and software provided by the Chandra X-ray Center. The National Radio Astronomy Observatory is a facility of the National Science Foundation operated under cooperative agreement by Associated Universities, Inc. This research has made use of NASA's Astrophysics Data System Bibliographic Services. This research has made use of data and/or software provided by the High Energy Astrophysics Science Archive Research Center (HEASARC), which is a service of the Astrophysics Science Division at NASA/GSFC. We acknowledge the use of public data from the Swift data archive.

This paper employs a list of *Chandra* datasets, obtained by the *Chandra* X-ray Observatory, contained in DOI: <https://doi.org/10.25574/cdc.196>.

## REFERENCES

- Berger, E., Keating, G. K., Margutti, R., et al. 2023, *ApJL*, 951, L31, doi: [10.3847/2041-8213/ace0c4](https://doi.org/10.3847/2041-8213/ace0c4)
- Bianciardi, G. and Ciccarelli A., M., Conzo, G., D'Angelo, M., et al. 2023, Multiband Photometry Evolution in the First Weeks of SN 2023ixf, a possible II-L Subtype Supernova, arXiv, doi: [10.48550/ARXIV.2307.05612](https://doi.org/10.48550/ARXIV.2307.05612)
- Bostroem, K. A., Pearson, J., Shrestha, M., et al. 2023, arXiv e-prints, arXiv:2306.10119, doi: [10.48550/arXiv.2306.10119](https://doi.org/10.48550/arXiv.2306.10119)
- Cardelli, J. A., Clayton, G. C., & Mathis, J. S. 1989, *ApJ*, 345, 245, doi: [10.1086/167900](https://doi.org/10.1086/167900)
- Chandra, P. 2018, *SSRv*, 214, 27, doi: [10.1007/s11214-017-0461-6](https://doi.org/10.1007/s11214-017-0461-6)
- Chevalier, R. A., & Fransson, C. 2017, in *Handbook of Supernovae*, ed. A. W. Alsabti & P. Murdin, 875, doi: [10.1007/978-3-319-21846-5\\_34](https://doi.org/10.1007/978-3-319-21846-5_34)
- Fabian, A. C., Iwasawa, K., Reynolds, C. S., & Young, A. J. 2000, *PASP*, 112, 1145, doi: [10.1086/316610](https://doi.org/10.1086/316610)
- Fransson, C., Lundqvist, P., & Chevalier, R. A. 1996, *ApJ*, 461, 993, doi: [10.1086/177119](https://doi.org/10.1086/177119)
- Gal-Yam, A., Arcavi, I., Ofek, E. O., et al. 2014, *Nature*, 509, 471, doi: [10.1038/nature13304](https://doi.org/10.1038/nature13304)
- Grefenstette, B. W., Brightman, M., Earnshaw, H. P., Harrison, F. A., & Margutti, R. 2023, *ApJL*, 952, L3, doi: [10.3847/2041-8213/acdf4e](https://doi.org/10.3847/2041-8213/acdf4e)
- Hiramatsu, D., Tsuna, D., Berger, E., et al. 2023, arXiv e-prints, arXiv:2307.03165, doi: [10.48550/arXiv.2307.03165](https://doi.org/10.48550/arXiv.2307.03165)
- Itagaki, K. 2023, *Transient Name Server Discovery Report*, 2023-39, 1
- Jacobson-Galan, W. V., Dessart, L., Margutti, R., et al. 2023, arXiv e-prints, arXiv:2306.04721, doi: [10.48550/arXiv.2306.04721](https://doi.org/10.48550/arXiv.2306.04721)
- Jencson, J. E., Pearson, J., Beasor, E. R., et al. 2023, *ApJL*, 952, L30, doi: [10.3847/2041-8213/ace618](https://doi.org/10.3847/2041-8213/ace618)
- Kilpatrick, C. D., Foley, R. J., Jacobson-Galán, W. V., et al. 2023, *ApJL*, 952, L23, doi: [10.3847/2041-8213/ace4ca](https://doi.org/10.3847/2041-8213/ace4ca)
- Kochanek, C. S. 2019, *MNRAS*, 483, 3762, doi: [10.1093/mnras/sty3363](https://doi.org/10.1093/mnras/sty3363)
- Lundquist, M., O'Meara, J., & Walawender, J. 2023, *Transient Name Server AstroNote*, 160, 1
- Makishima, K. 1986, in *The Physics of Accretion onto Compact Objects*, ed. K. O. Mason, M. G. Watson, & N. E. White, Vol. 266 (Springer-Verlag), 249, doi: [10.1007/3-540-17195-9\\_14](https://doi.org/10.1007/3-540-17195-9_14)
- Matt, G., Perola, G. C., & Piro, L. 1991, *A&A*, 247, 25
- Matthews, D., Margutti, R., AJ, N., et al. 2023, *The Astronomer's Telegram*, 16091, 1
- Mewe, R., Lemen, J. R., & van den Oord, G. H. J. 1986, *A&AS*, 65, 511
- Niu, Z.-X., Sun, N.-C., Maund, J. R., et al. 2023, arXiv e-prints, arXiv:2308.04677, doi: [10.48550/arXiv.2308.04677](https://doi.org/10.48550/arXiv.2308.04677)
- Panjkov, S., Auchettl, K., Shappee, B. J., et al. 2023, arXiv e-prints, arXiv:2308.13101, doi: [10.48550/arXiv.2308.13101](https://doi.org/10.48550/arXiv.2308.13101)
- Perley, D. A., Gal-Yam, A., Irani, I., & Zimmerman, E. 2023, *Transient Name Server AstroNote*, 119, 1
- Pledger, J. L., & Shara, M. M. 2023, arXiv e-prints, arXiv:2305.14447, doi: [10.48550/arXiv.2305.14447](https://doi.org/10.48550/arXiv.2305.14447)

- Quataert, E., & Shiode, J. 2012, MNRAS, 423, L92, doi: [10.1111/j.1745-3933.2012.01264.x](https://doi.org/10.1111/j.1745-3933.2012.01264.x)
- Riess, A. G., Yuan, W., Macri, L. M., et al. 2022, ApJL, 934, L7, doi: [10.3847/2041-8213/ac5c5b](https://doi.org/10.3847/2041-8213/ac5c5b)
- Schlafly, E. F., & Finkbeiner, D. P. 2011, ApJ, 737, 103, doi: [10.1088/0004-637X/737/2/103](https://doi.org/10.1088/0004-637X/737/2/103)
- Schlegel, D. J., Finkbeiner, D. P., & Davis, M. 1998, ApJ, 500, 525, doi: [10.1086/305772](https://doi.org/10.1086/305772)
- Singh Teja, R., Singh, A., Basu, J., et al. 2023, arXiv e-prints, arXiv:2306.10284, doi: [10.48550/arXiv.2306.10284](https://doi.org/10.48550/arXiv.2306.10284)
- Smith, N., & Arnett, W. D. 2014, ApJ, 785, 82, doi: [10.1088/0004-637X/785/2/82](https://doi.org/10.1088/0004-637X/785/2/82)
- Smith, N., Pearson, J., Sand, D. J., et al. 2023, arXiv e-prints, arXiv:2306.07964, doi: [10.48550/arXiv.2306.07964](https://doi.org/10.48550/arXiv.2306.07964)
- Soraisam, M. D., Szalai, T., Van Dyk, S. D., et al. 2023, arXiv e-prints, arXiv:2306.10783, doi: [10.48550/arXiv.2306.10783](https://doi.org/10.48550/arXiv.2306.10783)
- Torrejón, J. M., Schulz, N. S., Nowak, M. A., & Kallman, T. R. 2010, ApJ, 715, 947, doi: [10.1088/0004-637X/715/2/947](https://doi.org/10.1088/0004-637X/715/2/947)
- Van Dyk, S. D., Srinivasan, S., Andrews, J. E., et al. 2023, arXiv e-prints, arXiv:2308.14844, doi: [10.48550/arXiv.2308.14844](https://doi.org/10.48550/arXiv.2308.14844)
- Vasylyev, S. S., Yang, Y., Filippenko, A. V., et al. 2023, ApJL, 955, L37, doi: [10.3847/2041-8213/acf1a3](https://doi.org/10.3847/2041-8213/acf1a3)
- Yamanaka, M., Fujii, M., & Nagayama, T. 2023, arXiv e-prints, arXiv:2306.00263, doi: [10.48550/arXiv.2306.00263](https://doi.org/10.48550/arXiv.2306.00263)
- Yaron, O., Perley, D. A., Gal-Yam, A., et al. 2017, Nature Physics, 13, 510, doi: [10.1038/nphys4025](https://doi.org/10.1038/nphys4025)
- Zhang, J., Lin, H., Wang, X., et al. 2023, arXiv e-prints, arXiv:2309.01998, doi: [10.48550/arXiv.2309.01998](https://doi.org/10.48550/arXiv.2309.01998)
- Zimmerman, E. A., Irani, I., Chen, P., et al. 2023, arXiv e-prints, arXiv:2310.10727, doi: [10.48550/arXiv.2310.10727](https://doi.org/10.48550/arXiv.2310.10727)